

Numerically Stable Resonating Hartree-Fock

Erica Roy Miller¹ and Shane M. Parker^{1, a)}

*Department of Chemistry, Case Western Reserve University
10900 Euclid Ave, Cleveland, OH 44106, USA*

(Dated: 14 March 2025)

The simulation of excited states at low computational cost remains an open challenge for electronic structure (ES) methods. While much attention has been given to orthogonal ES methods, relatively little work has been done to develop nonorthogonal ES methods for excited states, particularly those involving nonorthogonal orbital optimization. We present here a numerically stable formulation of the Resonating Hartree-Fock (ResHF) method that uses the matrix adjugate to remove numerical instabilities in ResHF arising from nearly orthogonal orbitals, and we demonstrate improvements to ResHF wavefunction optimization as a result. We then benchmark the performance of ResHF against Complete Active Space Self-Consistent Field in the avoided crossing of LiF, the torsional rotation of ethene, and the singlet-triplet energy gaps of a selection of small molecules. ResHF is a promising excited state method because it incorporates the orbital relaxation of state-specific methods, while retaining the correct state crossings of state-averaged approaches. Our open-source ResHF implementation, *yucca*, is available on GitLab.

I. INTRODUCTION

One of the most powerful tools for unraveling ultrafast photodynamic processes is nonadiabatic molecular dynamics (NAMD). These simulations produce “molecular movies”, depicting the response of nuclei and electrons to incident light at femtosecond-to-picosecond timescales. NAMD simulations have been applied to the study of many diverse photodynamic processes, from intersystem crossings,^{1,2} to charge transfers,^{3,4} to internal conversions through conical intersections.^{5,6} The quality of an NAMD simulation is highly dependent on the underlying electronic structure method selected to provide electronic energies, nuclear forces, and nonadiabatic coupling vectors.⁷⁻⁹ The ideal electronic structure method for use with NAMD simulations would (i) be computationally efficient, (ii) generate correct conical intersections, (iii) treat states of different character with consistent accuracy, and (iv) reliably converge throughout the dynamics. Unfortunately, finding such a method is challenging, as excited states remain a frontier of electronic structure method development.

Time-dependent density functional theory (TDDFT) is widely used due to its favorable cost-to-accuracy ratio for excited states. However, there are several well-known deficiencies of TDDFT, including a fundamental neglect of double excitations¹⁰ and incorrect dimensionality of conical intersections between ground and excited states.¹⁰⁻¹² A state-averaged (SA) approach to complete active space self-consistent field (CASSCF) will properly reproduce conical intersections. However, SA-CASSCF is known to produce low accuracy charge transfer states,^{13,14} and perturbative corrections are often applied to remedy this. Alternatively, a state-specific (SS) approach to CASSCF has been shown achieve qualitatively accurate charge transfer states without the need to resort to expensive perturbative corrections.¹⁴ This is because SS-CASSCF allows for orbital relaxation tailored to an individual electronic state, while SA-CASSCF is unable to

efficiently accommodate the demands of different electronic environments. However, excited state SS-CASSCF solutions can be difficult to converge, and can disappear along a potential energy surface.^{15,16} Further, couplings between different electronic states, such as transition moments or nonadiabatic couplings, are difficult to obtain from SS solutions. The dilemma of CASSCF then is its inability to simultaneously achieve correct conical intersections and qualitatively accurate charge transfer states without resorting to large active spaces or perturbative corrections.

We posit here that the Resonating Hartree-Fock (ResHF)^{17,18} method resolves this tension between state-specific accuracy and state-averaged stability. The ResHF wavefunction is a linear combination of nonorthogonal Slater determinants. ResHF solutions are obtained by simultaneously optimizing the orbitals comprising these Slater determinants, as well as the state expansion coefficients. ResHF is one of many electronic structure methods¹⁹⁻²¹ that fall under the general strategy of nonorthogonal configuration interaction (NOCI). The unifying mantra of NOCI methods is “different orbitals for different states”. NOCI methods have been shown to capture large amounts of electron correlation with a compact configurational expansion of the wavefunction.^{19,22,23} ResHF in particular is able to further reduce the wavefunction size²⁴ and improve excited state energies²⁵ due to the incorporation of orbital relaxation. ResHF can be framed as a nonorthogonal analogue of CASSCF,²⁶ where the constraint of orthogonality between orbitals from different Slater determinants has been lifted. One of our main objectives in this contribution is to demonstrate that the resulting increase in flexibility allows ResHF to accommodate electronic states of different character in an unbiased manner via state-averaging.

However, variationally optimizing ResHF wavefunctions is notoriously difficult,^{23,24} raising concerns about the practicality of the method beyond model systems and small organic molecules. Recently, Mahler and Thompson shed light on underlying numerical instabilities present in ResHF.²⁶ In short, one of the key quantities in ResHF is the inverse of the interdeterminant overlap matrix, which becomes singular and thus numerically unstable when two determinants are (nearly)

^{a)}Electronic mail: shane.parker@case.edu

orthogonal.¹⁸ Mahler and Thompson addressed this by using generalized functions to compute orbital derivatives at these points of discontinuity.²⁶ In this contribution, we present an alternative solution: redefining the ResHF density matrix in terms of the matrix adjugate.^{27,28} The resulting formulation of orbital gradients between nonorthogonal Slater determinants is consistent with contributions by Koch and Dalgaard,²⁹ and more recent work by Chen and Scuseria,³⁰ although the approach and context here are distinct. Our ResHF implementation is available in our open-source, C++ software package, yucca.³¹

This paper is organized as follows. In Section II, we review the ResHF method, detailing the matrix adjugate based reformulation, ResHF-adj. In Section III, we discuss details of our ResHF implementation and benchmarking methodology. In Section IV we demonstrate the numerical stability of ResHF-adj in the context of wavefunction optimization. In Section V, we benchmark the performance of ResHF against SA/SS-CASSCF in the avoided crossing of LiF, the torsional rotation of ethene, and the singlet-triplet energy gaps of a selection of small to medium molecules from the QUEST database. We conclude in Section VI with some projections about future development of ResHF for excited states.

II. STABILIZING RESONATING HARTREE-FOCK WITH THE MATRIX ADJUGATE

We start by rewriting Fukutome’s original ResHF derivation¹⁸ with notation based on Burton.³² We refer the interested reader to these excellent papers for a more thorough treatment of the theory. Then we examine nonorthogonal orbitals in the limit of orthogonality as a primary source of numerical instability and show how the application of the matrix adjugate avoids this issue. We will use the following notation throughout: Atomic orbitals (AOs) are designated with indices $\mu\nu\lambda\sigma$, general molecular orbitals (MOs) are assigned indices $pqrs$, with occupied MOs $ijkl$ and virtual MOs ab . Slater determinants are labeled with AB , and ResHF electronic states with IJ . Matrices are represented using bold font. By default, these matrices are represented in the AO basis. Matrices represented in the MO basis are denoted using subscripted labels: ‘o’ for occupied and ‘u’ for virtual (unoccupied) MOs.

A. Resonating Hartree-Fock (ResHF) Theory

The ResHF wavefunction,

$$|\Psi_I\rangle = \sum_A c_{AI} |\Phi_A\rangle, \quad (1)$$

is a linear combination of nonorthogonal Slater determinants, $|\Phi_A\rangle$, where c_{AI} are the state expansion coefficients. Each Slater determinant has its own set of MOs that we express in the AO basis as

$$\phi_p^A(x) = \sum_\mu \chi_\mu(x) C_{\mu p}^A, \quad (2)$$

where χ_μ are spin AO basis functions, and $C_{\mu p}^A$ are the MO expansion coefficients for Slater determinant A . The MOs within a Slater determinant are orthonormal, while the MOs in different Slater determinants are allowed (not required) to be nonorthogonal.

The ResHF energy of state I , E_I , is defined as

$$E_I = \langle \Psi_I | \hat{H} | \Psi_I \rangle = \sum_{AB} c_{AI}^* \langle \Phi_A | \hat{H} | \Phi_B \rangle c_{BI}, \quad (3)$$

where the Hamiltonian operator is

$$\hat{H} = \sum_{\mu\nu} h_{\mu\nu} \hat{a}_\mu^\dagger \hat{a}_\nu + \frac{1}{2} \sum_{\mu\nu\lambda\sigma} [\mu\lambda | \nu\sigma] \hat{a}_\mu^\dagger \hat{a}_\nu^\dagger \hat{a}_\sigma \hat{a}_\lambda. \quad (4)$$

Here, $h_{\mu\nu}$ is a matrix element of the one-electron operator (containing kinetic energy and nuclear-electron attraction) and

$$[\mu\lambda | \nu\sigma] = \iint d\mathbf{x}_1 d\mathbf{x}_2 \chi_\mu^*(\mathbf{x}_1) \chi_\lambda(\mathbf{x}_1) \hat{r}_{12}^{-1} \chi_\nu^*(\mathbf{x}_2) \chi_\sigma(\mathbf{x}_2) \quad (5)$$

is a matrix element of the electron-electron repulsion, called electron repulsion integrals (ERI). In the above, we use square brackets to emphasize that the AOs contain spin degrees of freedom. In defining the creation and annihilation operators, \hat{a}_μ^\dagger and \hat{a}_μ , we follow the notation of Burton.³²

We now define several key intermediates used to compute matrix elements between nonorthogonal Slater determinants. First, $s_{AB} \equiv \langle \Phi_A | \Phi_B \rangle$ is the interdeterminant overlap, which is the determinant of the overlap matrix between the occupied MOs of Slater determinants A and B ,

$$s_{AB} = |\mathbf{S}_{oo}^{AB}|, \quad (6)$$

where

$$\mathbf{S}_{oo}^{AB} = \mathbf{C}_o^{A,\dagger} \mathbf{S} \mathbf{C}_o^B, \quad (7)$$

and \mathbf{S} is the AO overlap matrix. For convenience, our implementation retains a full complement of virtual MOs for each Slater determinant, in which case \mathbf{S}_{oo}^{AB} is the occupied-occupied block of the MO overlap matrix,

$$\mathbf{S}^{AB} = \mathbf{C}^{A,\dagger} \mathbf{S} \mathbf{C}^B = \begin{bmatrix} \mathbf{S}_{oo}^{AB} & \mathbf{S}_{ou}^{AB} \\ \mathbf{S}_{uo}^{AB} & \mathbf{S}_{uu}^{AB} \end{bmatrix}, \quad (8)$$

The interdeterminant one-body density matrix, $\gamma_{\mu\nu}^{AB} \equiv \langle \Phi_A | \hat{a}_\mu^\dagger \hat{a}_\nu | \Phi_B \rangle$, is

$$\gamma_{\mu\nu}^{AB} = s_{AB} \mathbf{C}_o^B (\mathbf{S}_{oo}^{AB})^{-1} \mathbf{C}_o^{A,\dagger} = s_{AB} \mathbf{Q}^{AB}, \quad (9)$$

where we have implicitly defined \mathbf{Q}^{AB} . The interdeterminant two-body density matrix is,

$$\begin{aligned} \Gamma_{\lambda\mu\sigma\nu}^{AB} &= \langle \Phi_A | \hat{a}_\mu^\dagger \hat{a}_\nu^\dagger \hat{a}_\sigma \hat{a}_\lambda | \Phi_B \rangle \\ &= s_{AB} \left[\mathcal{Q}_{\lambda\mu}^{AB} \mathcal{Q}_{\sigma\nu}^{AB} - \mathcal{Q}_{\sigma\mu}^{AB} \mathcal{Q}_{\lambda\nu}^{AB} \right]. \end{aligned} \quad (10)$$

With these definitions, the coupling matrix element, $H_{AB} \equiv \langle \Phi_A | \hat{H} | \Phi_B \rangle$ can be computed as

$$H_{AB} = \langle \mathbf{h} \gamma^{AB} \rangle + \frac{1}{2} \langle \mathbf{V} \Gamma^{AB} \rangle = \langle \mathbf{h} \gamma^{AB} \rangle + \frac{1}{2} \langle \mathbf{G}^{AB} \gamma^{AB} \rangle, \quad (11)$$

where $\langle \cdot \rangle$ is the matrix trace, $V_{\mu\lambda\nu\sigma} = [\mu\lambda|\nu\sigma]$, and

$$G_{\mu\nu}^{AB} = \sum_{\lambda\sigma} [\mu\nu||\lambda\sigma] Q_{\sigma\lambda}^{AB} \quad (12a)$$

$$[\mu\nu||\lambda\sigma] = [\mu\nu|\lambda\sigma] - [\mu\sigma|\lambda\nu]. \quad (12b)$$

We note here that Fukutome¹⁸ originally defined \mathbf{Q}^{AB} as the interdeterminant density matrix, instead of γ^{AB} . Similar definitions of \mathbf{Q}^{AB} have been used by Broer and Nieuwpoort,³³ and more recently by Mahler and Thompson²⁶ and Burton,³² with variant definitions to handle the cases when \mathbf{S}_{oo}^{AB} becomes singular. We omit these variant definitions here, addressing this issue via the matrix adjugate in Section II B.

The distinguishing feature of ResHF is the variational minimization of the energy with respect to both the MO expansion coefficients, $\{C^A\}$, and the ResHF state expansion coefficients, $\{c_{AI}\}$. To this end, we use a Lagrangian,

$$\mathcal{L} = E^{ResHF} - \sum_{IJ} N_{IJ} [\langle \Psi_I | \Psi_J \rangle - \delta_{IJ}], \quad (13)$$

where E^{ResHF} can be either single state or state averaged energy and N_{IJ} is a Lagrange multiplier that enforces orthonormality of the ResHF electronic states. The Lagrangian is made stationary when $N_{IJ} = \delta_{IJ} E_I w_I$, where w_I is the weight of state I , and the state expansion coefficients satisfy the generalized eigenvalue equation,

$$\mathbf{H}\mathbf{c} = \mathbf{s}\mathbf{e}\mathbf{E}, \quad (14)$$

where \mathbf{H} , \mathbf{c} , and \mathbf{s} are the matrix representations of the determinant coupling, state expansion coefficients, and determinant overlaps, respectively, and \mathbf{E} is a diagonal matrix of the energy eigenvalues. To optimize the MOs, we build a set of Resonating Fock matrices, shown here in the AO basis,

$$\mathbf{F}^A = \sum_I w_I \mathbf{F}_I^A \quad (15a)$$

$$\mathbf{F}_I^A = \mathbf{F}^{AA} |c_{AI}|^2 + \sum_{B \neq A} c_{AI}^* [\mathbf{K}^{AB} + (\mathbf{K}^{AB})^\dagger] c_{BI}, \quad (15b)$$

where we have defined the interdeterminant Fock matrix, $\mathbf{F}^{AB} = \mathbf{h} + \mathbf{G}^{AB}$. The \mathbf{K}^{AB} term can be written in the AO basis as

$$\mathbf{K}^{AB} = s_{AB} (\mathbf{1} - \mathbf{S} \mathbf{Q}^{AB}) \mathbf{F}^{AB} \mathbf{Q}^{AB} \mathbf{S} + (H_{AB} - s_{AB} E_I) \mathbf{S} \mathbf{Q}^{AB} \mathbf{S}. \quad (16)$$

Recognizing that \mathbf{Q}^{AB} is an oblique projector that maps occupied orbitals in A to occupied orbitals in B ,

$$\mathbf{Q}^{AB} \mathbf{S} \mathbf{Q}^{AB} = \mathbf{Q}^{AB}, \quad (17)$$

we see that \mathbf{K}^{AB} resembles a virtual-occupied projected Fock matrix. We conclude this section by observing the above ResHF equations simplify to the Hartree-Fock equations in the single Slater determinant case.

B. Overcoming Numerical Instability with the Matrix Adjugate

A fundamental question that arises when evaluating matrix elements involving nonorthogonal Slater determinants is what happens when the overlap between Slater determinants approaches zero? This question is particularly pressing for ResHF in particular, because orbital relaxation tends to push overlaps to be small but nonzero.²⁵ For a completely orthogonal pair of Slater determinants, \mathbf{S}_{oo}^{AB} is singular, meaning its inverse does not exist. Even when the overlap is small but nonzero, the condition number of \mathbf{S}_{oo}^{AB} becomes large, leading to numerical instability. Moreover, in the (near) singular case, the orbital gradients can become ill-defined, which would seem to preclude reliable convergence. From our perspective, this issue is an artifact of factoring out common intermediates like the determinant overlap.

The origin of numerical instability in ResHF can be illustrated with the singular value decomposition (SVD) of \mathbf{S}_{oo}^{AB} ,

$$\mathbf{S}_{oo}^{AB} = \mathbf{U}^{AB} \mathbf{\Sigma}^{AB} \mathbf{V}^{AB,\dagger}, \quad (18)$$

where \mathbf{U}^{AB} and \mathbf{V}^{AB} are unitary matrices, and $\mathbf{\Sigma}^{AB}$ is a diagonal matrix with singular values σ_i . As two Slater determinants become orthogonal, at least one singular value, σ_i , approaches zero, and the inverse, which contains $1/\sigma_i$, diverges. A common solution to this problem is to use different expressions according to the number of (near) zero singular values.²⁶ However, this approach leads to discontinuities in potential energy surfaces as the number of (near) zero singular values changes, and thus we do not further consider it here. An alternative approach is to apply a floor to the singular values using a user-selected cutoff, ε , such that $\sigma_i = \max(\sigma_i, \varepsilon)$. We will refer to this implementation strategy as ResHF-cutoff. Compared to the previous solution, the cutoff approach allows for some control of the numerical stability, should produce smooth potential energy surfaces, and is relatively straightforward to implement, albeit with a difficult-to-control loss of accuracy.

We argue that a better route is to reformulate ResHF in terms of the matrix adjugate, which can be defined for non-singular matrices as^{27,28}

$$\text{adj}(\mathbf{M}) \equiv |\mathbf{M}| (\mathbf{M})^{-1}. \quad (19)$$

Remarkably, even in the limit of singular \mathbf{M} the matrix adjugate remains well-defined. To clarify the connection to ResHF, recall that $s_{AB} = |\mathbf{S}_{oo}^{AB}|$, which lets us rewrite the ResHF density matrix in terms of the matrix adjugate,

$$\gamma^{AB} = \mathbf{C}_o^B \text{adj}(\mathbf{S}_{oo}^{AB}) \mathbf{C}_o^{A,\dagger}. \quad (20)$$

One of the key results of this paper is that ResHF energies and gradients can be rewritten in a numerically stable form using the matrix adjugate.

The matrix adjugate can be efficiently computed using the SVD of \mathbf{S}_{oo}^{AB} ,

$$\text{adj}(\mathbf{S}_{oo}^{AB}) = \eta \mathbf{V}^{AB} \mathbf{\Xi} \mathbf{U}^{AB,\dagger}, \quad (21)$$

where Ξ is a diagonal matrix with elements

$$\xi_i = \prod_{j \neq i} \sigma_j, \quad (22)$$

and $\eta = |\mathbf{U}^{AB}(\mathbf{V}^{AB})^\dagger| = \pm 1$. Here, we see why the matrix adjugate is well-defined in the limit of singular \mathbf{S}_{oo}^{AB} : the product of singular values contained in the matrix determinant cancels the division by singular value analytically, thus avoiding a numerical division by zero.

Using the above, γ^{AB} can be rewritten as

$$\gamma^{AB} = \eta \mathbf{B}_o \Xi^{AB} \mathbf{A}_o^\dagger, \quad (23)$$

where

$$\mathbf{A}_o = \mathbf{C}_o^A \mathbf{U}^{AB} \quad (24a)$$

$$\mathbf{B}_o = \mathbf{C}_o^B \mathbf{V}^{AB} \quad (24b)$$

form a biorthogonal basis. We note that the matrices \mathbf{A}_o and \mathbf{B}_o are of use only for the specific AB pair, but we omit AB superscripts for brevity.

To stabilize the ResHF energy, Eq. (3), using ResHF-adj, we turn our attention to the determinant coupling, H_{AB} . The one-electron contribution to H_{AB} can be straightforwardly stabilized by using Eq. (23) for the density matrix. For the two-electron contribution to H_{AB} , we express the ERIs in the SVD MO basis representation to get

$$\frac{1}{2} \langle \mathbf{G}^{AB} \gamma^{AB} \rangle = \eta \frac{1}{2} \sum_{ij} [i_A i_B || j_A j_B] \xi_{ij}, \quad (25)$$

where

$$\xi_{ij} = \frac{1}{\sigma_i} \frac{1}{\sigma_j} \prod_m \sigma_m. \quad (26)$$

Because of the diagonal terms, ξ_{ii} , this expression appears to be numerically unstable. However, the diagonal case here corresponds to self-interaction, which is exactly canceled. That is, $[i_A i_B || i_A i_B] = 0$, and thus ξ_{ii} will not contribute to the energy. We therefore define ξ_{ij} as

$$\xi_{ij} = \begin{cases} \prod_{m \neq i, j} \sigma_m & \text{if } i \neq j \\ \tau & \text{if } i = j \end{cases}, \quad (27)$$

where τ is a parameter. The cancellation of all terms involving ξ_{ii} means that the result should not depend on what value is used for τ . Indeed, we use this as a test of our implementation, and verify that the energies and gradients are identical for different values of τ . We default to setting $\tau = 1$.

We now turn our efforts to the Resonating Fock matrix, focusing on \mathbf{K}^{AB} . In the ResHF-cutoff approach, the \mathbf{K}^{AB} matrix can be computed directly in the AO basis (Eq. (16)), significantly simplifying the implementation. For ResHF-adj, we compute \mathbf{K}^{AB} in the SVD transformed MO basis,

$$\mathbf{A}^\dagger \mathbf{K}^{AB} \mathbf{A} = \begin{bmatrix} \mathbf{A}_o^\dagger \mathbf{K}^{AB} \mathbf{A}_o & \mathbf{A}_o^\dagger \mathbf{K}^{AB} \mathbf{A}_u \\ \mathbf{A}_u^\dagger \mathbf{K}^{AB} \mathbf{A}_o & \mathbf{A}_u^\dagger \mathbf{K}^{AB} \mathbf{A}_u \end{bmatrix} = \begin{bmatrix} \mathbf{K}_{oo}^{AB} & \mathbf{K}_{ou}^{AB} \\ \mathbf{K}_{uo}^{AB} & \mathbf{K}_{uu}^{AB} \end{bmatrix}, \quad (28)$$

where $\mathbf{A}_u = \mathbf{C}_u^A$ and $\mathbf{A}_o = \mathbf{C}_o^A \mathbf{U}^{AB}$. The \mathbf{K}_{ou}^{AB} and \mathbf{K}_{uo}^{AB} block matrices vanish because

$$\mathbf{Q}^{AB} \mathbf{S} \mathbf{A}_u = \mathbf{B}_o (\Sigma^{AB})^{-1} \mathbf{A}_o^\dagger \mathbf{S} \mathbf{A}_u = 0. \quad (29)$$

For the \mathbf{K}_{oo}^{AB} block matrix, we find

$$\mathbf{A}_o^\dagger (\mathbf{1} - \mathbf{S} \mathbf{Q}^{AB}) = \mathbf{A}_o^\dagger - \Sigma^{AB} (\Sigma^{AB})^{-1} \mathbf{A}_o^\dagger = 0 \quad (30a)$$

$$\mathbf{A}_o^\dagger \mathbf{S} \mathbf{Q}^{AB} \mathbf{S} \mathbf{A}_o = \Sigma^{AB} (\Sigma^{AB})^{-1} \mathbf{A}_o^\dagger \mathbf{S} \mathbf{A}_o = \mathbf{1}, \quad (30b)$$

where $\mathbf{1}$ is an $n_e \times n_e$ identity matrix, where n_e is the number of electrons. Therefore, the only surviving terms are

$$\mathbf{K}_{oo}^{AB} = (H_{AB} - s_{AB} E_I) \mathbf{1}. \quad (31)$$

Starting from

$$\mathbf{K}_{uo}^{AB} = s_{AB} \mathbf{A}_u^\dagger (\mathbf{1} - \mathbf{S} \mathbf{Q}^{AB}) \mathbf{F}^{AB} \mathbf{Q}^{AB} \mathbf{S} \mathbf{A}_o + (H_{AB} - s_{AB} E_I) \mathbf{A}_u^\dagger \mathbf{S} \mathbf{Q}^{AB} \mathbf{S} \mathbf{A}_o, \quad (32)$$

we group terms according to the number of inverse MO overlap matrices present to get

$$\begin{aligned} K_{ai}^{AB} &= \eta \left(\bar{h}_{ai}^{AB} - E_I \bar{s}_{ai}^{AB} \right) \xi_i \\ &+ \eta \sum_j \left(\bar{S}_{ai}^{AB} \bar{h}_{jj}^{AB} - \bar{S}_{aj}^{AB} \bar{h}_{ji}^{AB} + [a_A i_B || j_A j_B] \right) \xi_{ij} \\ &+ \eta \sum_{jk} \left(\frac{1}{2} \bar{S}_{ai}^{AB} [j_A j_B || k_A k_B] - \bar{S}_{aj}^{AB} [j_A i_B || k_A k_B] \right) \xi_{ijk}, \end{aligned} \quad (33)$$

where the one-electron potential and AO overlap matrices have been transformed into the SVD MO representation as

$$\bar{h}_{pq}^{AB} = \sum_{\mu\nu} A_{\mu p}^* h_{\mu\nu} B_{\nu q} \quad (34)$$

$$\bar{S}_{pq}^{AB} = \sum_{\mu\nu} A_{\mu p}^* S_{\mu\nu} B_{\nu q}, \quad (35)$$

and we introduced ξ_{ijk} as

$$\xi_{ijk} = \frac{1}{\sigma_i} \frac{1}{\sigma_j} \frac{1}{\sigma_k} \prod_m \sigma_m. \quad (36)$$

The first term in K_{ai}^{AB} is stable because ξ_i has no singular values in the denominator. The second term is stable because the summand vanishes when $i = j$, thus allowing us to use Eq. (27). The third term is also stable, but more challenging to see, so we will show it directly. To show that the third term is stable, it suffices to show that the summand will vanish when any two indices of ξ_{ijk} are equal, because we can then define ξ_{ijk} in analogy to Eq. (27). First, we see that the summand vanishes when $j = k$, because the antisymmetrized integrals vanish. Next, we symmetrize the summand with respect to j and k , and use this to restrict the summation to be

$$\sum_{j < k} \left(\bar{S}_{ai}^{AB} [j_A j_B || k_A k_B] - \bar{S}_{aj}^{AB} [j_A i_B || k_A k_B] - \bar{S}_{ak}^{AB} [k_A i_B || j_A j_B] \right) \xi_{ijk}, \quad (37)$$

where we have used the symmetry of the ERIs and ξ_{ijk} to simplify. Now we can see that when $j = i$, the first two terms of Eq. (37) cancel, and the third vanishes. Similarly, when $k = i$, the first and third terms cancel, and the second vanishes. Thus, every term in K_{ai}^{AB} is numerically stable. As a result, we redefine ξ_{ijk} as

$$\xi_{ijk} = \begin{cases} \prod_{m \neq i,j,k} \sigma_m & \text{if } i \neq j \neq k \\ \tau & \text{otherwise} \end{cases}, \quad (38)$$

where we use the same τ is in Eq. (27).

A major consequence of using this formulation is that it requires the ERIs to be computed in an MO basis, whereas Hartree–Fock implementations are often most efficient (partially) in the AO basis. To avoid a costly 4-index transformation of the ERIs, we use the resolution of the identity (RI) approximation^{34,35} for all ERIs,

$$(pq|rs) \approx \sum_{PQ} (pq|P)(P|Q)^{-1}(Q|rs), \quad (39)$$

where $(pq|P)$ and $(P|Q)$ are 3-center and 2-center ERIs, respectively, and PQ label auxiliary fitting basis functions. With the RI approximation, the overall scaling of the ResHF-adj method is $\mathcal{O}(N^5)$, where N is a measure of system size. By contrast, Hartree–Fock with the RI approximation scales as $\mathcal{O}(N^4)$.³⁶ The increase in scaling comes from the ξ_{ijk} terms, which complicate separation of terms. A detailed discussion of how RI was used to implement Eq. (33) is provided in Appendix A.

III. METHODOLOGY AND IMPLEMENTATION DETAILS

The matrix adjugate formulation of ResHF was implemented into our open-source code, yucca.³¹ All SA-CASSCF calculations were performed using ORCA version 5.0.0.³⁷ SS-CASSCF calculations for LiF were also performed with ORCA, while SS-CASSCF energies for ethene were obtained from Reference 16. All input files and data can be found in an Open Science Framework repository.³⁸

Default convergence criteria ($10^{-7} E_h$ energy change and $10^{-3} E_h$ orbital gradient) were used for all CASSCF calculations performed in ORCA. The first-order perturbative SuperCI method³⁹ was used to converge the CASSCF orbitals. To match the CASSCF convergence criteria, ResHF calculations were considered converged when the state-averaged energy changed by less than $10^{-7} E_h$ and the orbital gradient was below $10^{-3} E_h$, unless stated otherwise. The direct inversion of the iterative subspace (DIIS)⁴⁰ in combination with the maximum overlap method was used to converge the ResHF orbitals. For both the ethene and LiF scans, converged ResHF and CASSCF orbitals from the prior step were used as initial guesses for their respective methods.

The def2-SVP basis set⁴¹ was used in both the numerical stability analysis and LiF bond dissociation. The aug-cc-pVDZ basis set^{42,43} was used to compute the ethene torsional curve in order to be consistent with SS-CASSCF energies

from Reference 16. Vertical excitation energies of QUEST database molecules were computed using the def2-QZVP basis set.⁴⁴

All ResHF calculations were performed using unrestricted determinants. Detailed ResHF equations using unrestricted MOs can be found in Appendix B.

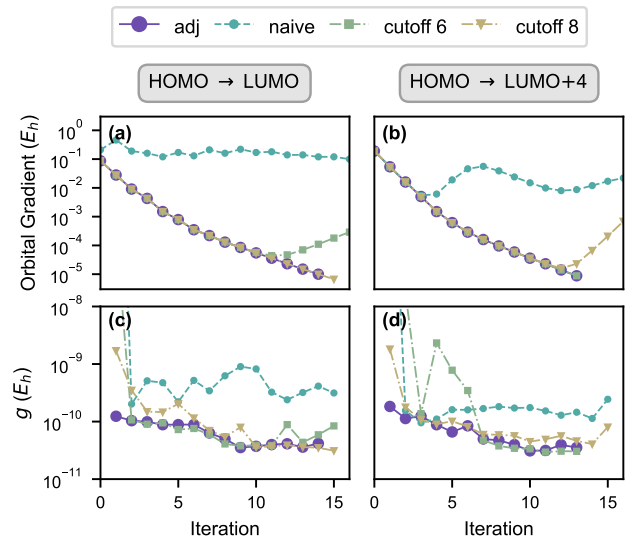


FIG. 1. Orbital gradient (a, b) and minimum Fock matrix error, g (c, d) as a function of iteration number for planar ethene using 3SA-ResHF(3sd)/def2-SVP. Two ResHF wavefunctions are compared: initialized from a HOMO \rightarrow LUMO single excitation (a, c) and initialized from a HOMO \rightarrow LUMO+4 single excitation (b, d). A tight orbital gradient threshold ($10^{-5} E_h$) was used. Consistent convergence and low Fock matrix errors are seen with matrix adjugate stabilized ResHF (purple), while unstabilized “naive” ResHF (teal) fails to converge due to large errors in the Fock matrix. ResHF with singular value cutoffs of 10^{-6} (green) and 10^{-8} (tan) perform inconsistently between ResHF wavefunction initializations.

IV. NUMERICAL ANALYSIS OF RESHF ALGORITHM STABILITY

To begin the analysis, we first compare the wavefunction optimization performances of the ResHF-adj and ResHF-cutoff implementations, using planar ethene. We compare two ResHF wavefunctions, each built from 3 Slater determinants: the HF ground state, an alpha-spin single excitation, and a beta-spin single excitation. For the first ResHF wavefunction, we initialize the determinants from single excitations from HOMO \rightarrow LUMO, while the second ResHF wavefunction is built from HOMO \rightarrow LUMO+4 single excitations, where HOMO and LUMO stand for highest occupied MO and lowest unoccupied MO, respectively. This initial guess ensures that Slater determinants are orthogonal for the initial wavefunction, meaning numerical instabilities are expected from the onset.

Three ResHF strategies are used to attempt to converge these wavefunctions: (i) a naive approach where no attempts

at mitigating numerical instability are made, (ii) the ResHF-cutoff approach, where a user set threshold, ϵ , is applied to small singular values, and (iii) the ResHF-adj approach. The progress of the optimizations are shown in Figure 1a and 1b. The naive approach dramatically fails to converge for either the HOMO \rightarrow LUMO or the HOMO \rightarrow LUMO+4 initial guesses. ResHF-adj, on the other hand, converges monotonically for both initial guesses. With the right cutoff, similar convergence behavior can be achieved using the ResHF-cutoff approach. However, we find that different initial guesses require different cutoffs for stable convergence. For example, in the HOMO \rightarrow LUMO case, $\epsilon = 10^{-8}$ converges, while $\epsilon = 10^{-6}$ fails to converge (Figure 1a). Yet we observe the opposite in the HOMO \rightarrow LUMO+4 case: $\epsilon = 10^{-6}$ converges, while $\epsilon = 10^{-8}$ does not (Figure 1b).

The differences in convergence performance can be understood from examining the errors present in the Resonating Fock matrices throughout the optimization process, as shown in Figures 1c and 1d. We assess the accuracy of the off-diagonal blocks of the Resonating Fock matrices by comparing to numerical orbital gradients obtained through finite difference, quantifying the error as

$$g_{err}(h) = \sqrt{\sum_{Aia} |F_{ia}^A - \frac{dE^{SA}}{d\kappa_{ai}^A}(h)|^2}, \quad (40)$$

where κ_{ai}^A is an orbital rotation between an occupied (ϕ_i^A) and virtual (ϕ_a^A) spin MO pair, and h represents the finite difference step size. Numerical orbital gradients were computed with a fourth order central finite difference stencil. To isolate the error in the Fock matrix from the error of the finite difference approximation, we compute the numerical gradient using step sizes ranging from 10^{-4} to 10^{-1} , and take the minimum, $g = \min_h g(h)$, as a proxy for the quality of the analytical gradients. We note that we use the matrix adjugate stabilized energy expression to compute the finite difference energies in all cases.

The approximate errors, g , are plotted for each SCF iteration in Figure 1c and 1d. ResHF-adj shows a *consistently* low level of error, sitting at or below $1.8 \times 10^{-10} E_h$ for each step of the optimization. The ResHF-cutoff approaches start off with several orders of magnitude larger errors than ResHF-adj at the first iteration, but significantly reduce these errors as the optimization progresses. However, there are seemingly random spikes in error for ResHF-cutoff throughout optimization. While these error spikes might appear minimal, they nevertheless can preclude convergence (Figure 1a and 1b).

V. BENCHMARKING EXCITED STATE RESONATING HARTREE-FOCK PERFORMANCE

In this section, we seek to examine the performance of ResHF against CASSCF. To orient the reader, we summarize here some key differences between these methods. In SS-CASSCF, a single set of molecular orbitals is optimized for a single electronic state. Because one set of orthonormal orbitals are used, the Slater determinants within the com-

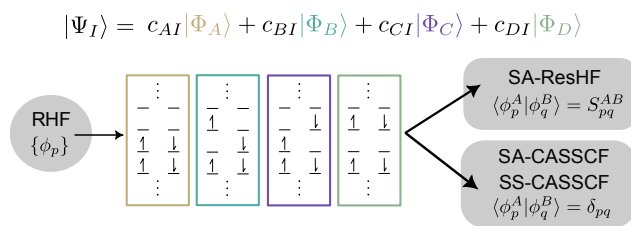


FIG. 2. Wavefunction initialization for ResHF and CASSCF methods. Initial orbitals were obtained from a restricted Hartree-Fock calculation, then used to build a 4 determinant active space. Three modes of orbital relaxation were then applied: SA-ResHF, SA-CASSCF, and SS-CASSCF. In CASSCF orbitals between determinants are constrained to remain orthonormal during orbital relaxation, while this constraint is lifted for ResHF.

plete active space are orthonormal. However, SS-CASSCF solutions for different electronic states are not orthogonal because they are the result of separate optimizations. Orthogonal electronic states can be recovered via state interaction⁴⁵, but this requires the evaluation of matrix elements between nonorthogonal Slater determinants. By contrast, SA-CASSCF ensures orthogonal electronic states by optimizing orbitals for an average of the electronic states. This can come at the cost of accuracy when using SA-CASSCF to describe electronic states of different character, such as charge transfer states.^{13,14} In our view, SA-ResHF is intermediate between SS-CASSCF and SA-CASSCF in the sense all electronic states are optimized simultaneously, but each Slater determinant has its own set of orbitals. Put another way, SA-ResHF can be obtained by removing the constraint of using a single set of orbitals from SA-CASSCF.

In the following, we show that SA-ResHF is about as accurate as SS-CASSCF, without sacrificing the benefits of state-averaging. We begin by examining the performance of SA-ResHF and SA/SS-CASSCF for charge transfer states with the bond dissociation of LiF, before examining the continuity of excited state surfaces along the torsional rotation of ethene. We will then apply minimal sized SA-ResHF and SA-CASSCF wavefunctions to compute singlet-triplet energy gaps of a selection of small molecules.

To allow for direct comparison between the methods, the same sized wavefunction was used for ResHF and CASSCF, unless otherwise specified. A sketch of the wavefunction initialization scheme is presented in Figure 2. Both CASSCF and ResHF initial guesses for molecular orbitals were obtained from restricted Hartree-Fock (RHF) calculations, unless otherwise specified. For SS/SA-CASSCF, a $(2e, 2o)$ active space was used, while a set of 4 Slater determinants were used to build the ResHF wavefunction. To mimic the full configuration interaction expansion of the CASSCF active space, the ResHF determinants were initialized as the closed-shell RHF determinant, a single alpha-spin electron excitation out of the RHF determinant, the paired beta-spin single electron excitation, and a double electron excitation (Figure 2). We will use the ResHF-adj implementation exclusively in the following analysis.

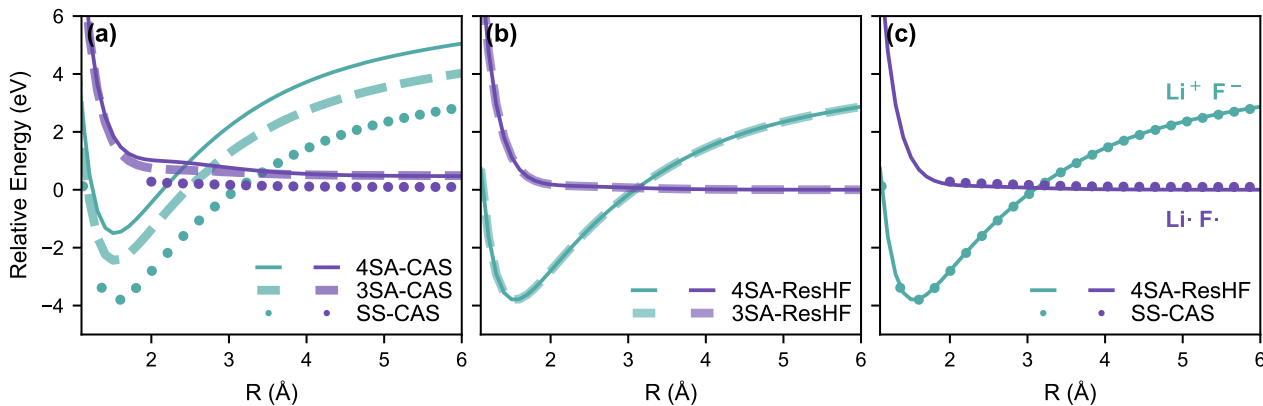


FIG. 3. The first two singlet states of the LiF bond dissociation. Energies are displayed relative to the UHF energy of LiF at a fully dissociated bond length (8.0 Å). All energies were computed using the def2-SVP basis set. Panel (a) compares SS-CASSCF(2e,2o) to 3SA and 4SA-CASSCF(2e,2o), panel (b) compares 3SA and 4SA-ResHF(4sd) energies, and panel (c) compares SS-CASSCF(2e,2o) and 4SA-ResHF(4sd).

A. Flexible ResHF Orbital Relaxation in LiF Dissociation

The LiF bond dissociation is a useful model to evaluate how well electronic structure methods can accommodate the contradictory demands of charge transfer and locally excited states. Marie and Burton¹⁵ have shown that several SS-CASSCF solutions exist for this system. We target two electronic states, one ionic and one neutral. This pair of states was referred to as “quasi-diabatic” by Marie and Burton¹⁵ because they exhibit a weakly avoided crossing. The S_0 state has ionic character at bond equilibrium and mixes with the diradical S_1 state as the LiF bond stretches.^{15,46,47} A state-averaged approach in CASSCF will attempt to describe both states with a single set of orbitals, which is challenging for a small active space. We also include the lowest lying triplet state in the state-averaging. Therefore, SA-CASSCF will tend to favor the diradical state over the ionic state during orbital relaxation, while SS-CASSCF will be free from this bias.

Applying the 4 determinant ResHF/CASSCF wavefunctions (Figure 2), we compute the LiF bond dissociation curve for the ionic and covalent singlet states. SA-CASSCF and SA-ResHF curves were generated by starting at a bond length of 8.0 Å and scanning at an interval of 0.1 Å. We ensured determinants were initialized to include the p orbital on the F atom that aligned with the LiF bond. For state-averaging schemes, we applied a 3SA equal weighting across ionic, covalent, and T_1 states and a 4SA equal weighting that also includes the high lying S_2 state. The SS-CASSCF covalent state was also obtained by starting at a fully dissociated 8.0 Å structure and using RHF MOs in the initial guess. Convergence failures occurred for the SS-CASSCF covalent state scan at lengths shorter than 2.0 Å. We attribute this to limitations of the default convergence routines we selected in ORCA, rather than a disappearance of the quasi-diabatic SS-CASSCF solution.¹⁵ To obtain the SS-CASSCF ionic state, the scan was started at a bond length of 1.6 Å. We also found it necessary to initialize the SS-CASSCF ionic wavefunction using the 3SA-CASSCF converged orbitals in order to ensure the ionic state did not

collapse to the covalent state near the crossing. For clarity, we have omitted the lowest lying T_1 state and the high energy S_2 state from Figure 3.

We compare the SA-CASSCF and SS-CASSCF potential energy surfaces in Figure 3a. SS-CASSCF, where orbitals are optimized to exclusively accommodate either the ionic or covalent state, yields the lowest energy surfaces and indicates a crossing near 3.1 Å. The 3SA-CASSCF approach raises the ionic state bond equilibrium energy by 1.4 eV and shifts the crossing point to 2.7 Å. Introducing the high energy S_2 state into the average (4SA-CASSCF) further deteriorates the quality of the potential energy surfaces, raising the bond equilibrium energy by 2.4 eV and shifting the crossing point to 2.5 Å. In contrast, ResHF is insensitive to the number of states included in state-averaging (Figure 3b) and almost exactly reproduces the SS-CASSCF potential energy surfaces (Figure 3c). Thus, ResHF allows for tailored orbital relaxation for individual electronic states, while preserving the advantages of state averaging.

B. Well-Defined ResHF Surfaces in Ethene Torsional Scan

As powerful as an SS-CASSCF approach can be for excited states, a well-known issue is the disappearance of individual solutions along a potential energy surface. Recently, Saade and Burton¹⁶ have performed extensive analysis of the excited SS-CASSCF(2e, 2o) solutions of ethene during torsional rotation about the carbon-carbon double bond. Here, we compare the performance of SS-CASSCF in ethene to SA-ResHF and SA-CASSCF, to demonstrate the stability of a state-averaged approach.

With the CASSCF(2e, 2o) and ResHF(4sd) wavefunctions, we are able to model three low-lying excited states of interest: the triplet $\pi \rightarrow \pi^*$ excitation, which is commonly denoted as T in Mulliken labeling, the singlet $\pi \rightarrow \pi^*$ single excitation (V), and the double $(\pi)^2 \rightarrow (\pi^*)^2$ excitation ionic state (Z). The ionic Z state, with a vertical excitation energy around 13

eV at a planar geometry, dramatically reduces in energy as ethene undergoes torsional rotation, becoming strongly coupled to the V state at the 90-degree torsional rotation.⁴⁸ The V state is a particularly challenging state to accurately model owing to its much more diffuse nature than its triplet counterpart, the T state.⁴⁹

Starting from the 90 degree twisted structure, we initialize the ResHF determinants with single and double excitations from the highest occupied and lowest unoccupied RHF molecular orbitals. An equal weight state averaging scheme was applied across the three singlet states and one triplet state for both CASSCF and ResHF. From the 90 degree structure, we scan towards planar ethene at an interval of 0.05 degrees. The resulting energy surfaces are shown in Figure 4.

Little deviation is observed between SA-ResHF, SA-CASSCF, and SS-CASSCF potential energy surfaces. The largest deviation between SA-CASSCF and SA-ResHF is observed at the planar ethene structure, with SA-ResHF coming in 0.5 eV higher in energy for the T state and 0.3 eV lower for the V state, relative to SA-CASSCF. SA-ResHF and SA-CASSCF produce qualitatively similar, yet visually distinct electronic density differences at this planar geometry (Figure S1), which likely explains the energetic differences. Notably, neither SA-ResHF nor SA-CASSCF captures the more compact nature of the T state compared to the V state. SS-CASSCF solutions do capture this distinction¹⁶, indicating that SA-ResHF may not be as efficient at capturing orbital relaxation as SS-CASSCF.

The most striking feature of Figure 4 is the disappearance of the SS-CASSCF V state at 40 degrees. Saade and Burton¹⁶ attribute this to the coalescence of two SS-CASSCF solutions, resulting in a pair annihilation point. On the other hand, both SA-CASSCF and SA-ResHF produce a continuous V state energy surface across the full torsional rotation. The V state is thought to be essential for a prominent internal conversion pathway of photoexcited ethene to the ground state.⁵⁰ The continuity of the excited state surfaces along ethene’s torsional rotation is therefore a significant advantage of state-averaged approaches in the context of photodynamics applications.

C. High Quality ResHF Singlet-Triplet Gaps

Accurate singlet-triplet state energy gaps (ΔE_{ST}) are essential for intersystem crossing. Even small organic molecules with minimal spin-orbit couplings can exhibit ultrafast intersystem crossings given small enough ΔE_{ST} .^{1,2} To survey the performance of ResHF for ΔE_{ST} , we compute the lowest lying singlet and triplet excited states for a set of nine molecules taken from the QUEST database^{51–53}. We apply an equal weight 3SA scheme across the S_0 , S_1 , and T_1 states for both CASSCF and ResHF calculations. To select the initial guess, we first compute configuration interaction singles calculations of the S_1 state to identify the largest occupied-to-virtual single excitation contribution from the RHF orbitals. The subsequent occupied-virtual orbital pair was used to build the CASSCF and ResHF initial wavefunctions, as shown in Figure 2.

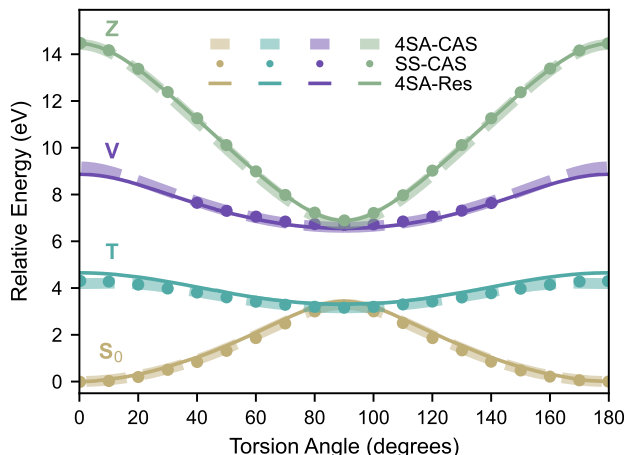


FIG. 4. Torsional scan about the carbon-carbon bond of ethene, showing the singlet ground state and the T, V, and Z excited states. 4SA-ResHF(4sd) and 4SA-CASSCF(2e,2o) energies were computed using the aug-cc-pVDZ basis set. SS-CASSCF(2e,2o) energies were digitized from Reference 16. Energies are displayed as relative to the S_0 energy of planar ethene computed by the respective electronic structure method.

For the “larger” molecules (pyrimidine, benzothiadiazole, benzoxadiazole), ResHF convergence failures were observed when using the 4 Slater determinant wavefunction. Steady decreases in energy were observed for the first 10 optimization cycles before reaching a plateau. After about 50 more cycles, large spikes in energy occur. We hypothesize this is due to the relatively naive convergence strategy used here (simple DIIS). Second order, or quasi-second order, convergers are commonly applied to CASSCF wavefunction optimization, and thus we expect the same will be required to more reliably converge ResHF for a broader range of systems.

ResHF convergence improved significantly upon omission of the doubly excited determinant. Therefore, Table I displays results from a 3SA-ResHF(3sd) wavefunction. 4SA-ResHF(4sd) energies for the smaller molecules can be found in the Supplementary Materials. We emphasize that this reduction of the ResHF wavefunction expansion is motivated by convergence stability, *not* computational expense. ResHF scales as $\mathcal{O}(N^2)$ with respect to the number of Slater determinants in the expansion.

In comparing the vertical excitation energies to the theoretical best estimates (TBEs), it is clear that both ResHF(3sd) and CASSCF(2e, 2o) are far from achieving quantitative accuracy with such a small active space. 3SA-CASSCF shows a 0.97 eV mean absolute error (MAE) for triplet states and a 0.70 eV MAE for singlet states. 3SA-ResHF has slightly lower MAEs, with 0.75 eV for triplet states and 0.66 eV for singlet states.

However, ResHF significantly improves over CASSCF for predicting ΔE_{ST} , with an MAE of 0.27 eV to CASSCF’s 0.48 eV. This improvement occurs entirely at the neglect of dynamic correlation. Qualitative errors in state splittings in CASSCF are well-known. Conventionally, dynamical correlation is considered mandatory to reduce systematic errors in

TABLE I. Vertical excitation energies (in eV) for selected QUEST database molecules. 3SA-CASSCF(2e,2o) and 3SA-ResHF(3sd) energies were computed using the def2-QZVP basis set. $\langle S^2 \rangle$ values for ResHF states are shown in parentheses. Theoretical best estimates (TBE) obtained from QUEST are used to compute mean average errors (MAE). Singlet-triplet energy gaps are calculated as $\Delta E_{st} = E_{S_1} - E_{T_1}$.

Molecule	3SA-CASSCF			3SA-ResHF			TBE		
	E_{S_1}	E_{T_1}	ΔE_{st}	E_{S_1}	E_{T_1}	ΔE_{st}	E_{S_1}	E_{T_1}	ΔE_{st}
formaldehyde	3.07	2.47	0.60	2.75 (0.064)	2.40 (2.000)	0.35	3.97	3.58	0.39 ^a
acetaldehyde	3.41	2.86	0.56	3.12 (0.067)	2.80 (2.000)	0.32	4.31	3.98	0.33 ^a
formamide	4.45	4.01	0.44	4.38 (0.055)	4.12 (2.000)	0.26	5.63	5.37	0.26 ^a
streptocyanine-C1	8.25	5.36	2.88	7.27 (0.093)	5.70 (2.001)	1.58	7.12	5.52	1.60 ^a
acetone	3.58	3.05	0.53	3.31 (0.066)	3.01 (2.000)	0.30	4.48	4.15	0.33 ^b
cyclopentadiene	6.47	3.51	2.96	6.00 (0.027)	3.37 (2.000)	2.63	5.55	3.31	2.24 ^b
pyrimidine	5.35	4.97	0.38	4.61 (0.454)	4.43 (2.011)	0.18	4.45	4.10	0.35 ^b
benzoxadiazole	5.60	2.99	2.61	3.95 (0.347)	3.15 (2.009)	0.80	4.52	2.74	1.78 ^c
benzothiadiazole	5.00	2.90	2.10	3.69 (0.210)	3.06 (2.004)	0.63	4.23	2.82	1.41 ^c
MAE	0.97	0.70	0.48	0.75	0.66	0.27			

^a Theoretical best estimates (TBE) taken from QUEST subset #1 (Ref. 51)

^b Theoretical best estimates (TBE) taken from QUEST subset #3 (Ref. 52)

^c Theoretical best estimates (TBE) taken from QUEST subset #7 (Ref. 53)

singlet-triplet gaps⁵⁴ and beyond.^{13,55,56} Our results suggest that *relaxation* may be more important than dynamical correlation in this context. This fits with conclusions drawn by Tran and Neuscammann,¹⁴ who showed that SS-CASSCF can dramatically reduce systematic errors in SA-CASSCF calculations of charge-transfer states.

In examining the ResHF wavefunctions, we commonly find that each ResHF electronic state is predominantly described by one or two Slater determinants. Direct comparison of orbitals between ResHF and CASSCF is not straightforward, as ResHF has multiple sets of orbitals. We therefore computed electronic density differences for each S_1 and T_0 state. Visualizations of these for all molecules in Table I can be found in the Supplementary Materials. In all cases, the density differences from SA-CASSCF and SA-ResHF are qualitatively similar, indicating that the same electronic states were found by both methods. However, small deviations in these density differences may have surprisingly large impacts on the state-splittings. For instance, in streptocyanine, SA-ResHF underestimates the ΔE_{ST} gap by 0.02 eV, while SA-CASSCF overestimates this same gap by 1.28 eV. Yet, their density differences appear qualitatively similar (Figure S5). In another example, signatures of orbital relaxation are evident in the SA-ResHF density differences for benzoxadiazole and benzothiadiazole in the form of a negative band in the plane of the ring (Figures S9 and S10). Interestingly, while SA-CASSCF overestimates these ΔE_{ST} gaps, SA-ResHF underestimates them.

Of course, the current benchmark set is limited in scope due to limitations in ResHF convergence. Further investigations on the ability of ResHF to overcome state splitting errors traditionally attributed to a lack of dynamic correlation across a wider benchmark set of molecules is ongoing in our group.

Finally, we note that the largest errors in ΔE_{ST} for SA-ResHF occur for pyrimidine, benzoxadiazole, and benzothiadiazole in which we also observed notable spin contamination in the singlet states. See the Supplemental Materials for a derivation of $\langle S^2 \rangle$. In our view, the increased spin contamination is likely a symptom pointing to the presence of additional

static correlation in these systems that cannot be captured with a 3 Slater determinant expansion, which may be mitigated by more robust initial guesses. Spin contamination can also be entirely eliminated by using a set of spin-restricted determinants to build the ResHF wavefunction. Work towards this end is ongoing in our group.

VI. CONCLUSIONS AND FUTURE OUTLOOK

In this paper, we have presented a numerically stable reformulation of the ResHF method. The matrix adjugate ResHF implementation, enabled by the resolution-of-the-identity approximation, effectively uses the determinant of the molecular orbital overlap matrix to remove numerical instabilities encountered when attempting to take the inverse of a nearly singular overlap matrix. The results shown here are consistent with recent efforts by Chen and Scuseria to eliminate numerical instabilities in the Hartree-Fock-Bogoliubov method.³⁰ Our implementation is freely available in the open-source code, *yucca*.³¹

Using the ResHF-adj implementation, we have benchmarked the performance of ResHF against CASSCF in several systems. We showed that ResHF is free from state biasing errors observed in SA-CASSCF in the avoided crossing arising from LiF bond dissociation. In fact, the SA-ResHF energy surfaces for the ionic and covalent LiF states map on directly to the SS-CASSCF energy surfaces. We also showed that SA-ResHF is able to produce continuous excited state energy surfaces in the torsional rotation about the carbon-carbon bond of ethene, in contrast with recently reported SS-CASSCF results. These two results in particular lead us to conclude that ResHF is able to unite the energetic benefits of state-specific methods with the reliability of state-averaged approaches. We closed with a comparison between ResHF and CASSCF singlet-triplet energy gaps, showing that a similarly sized ResHF wavefunction can significantly outperform CASSCF, albeit hindered by spin contamination.

Moving forward, we see several avenues for improvement in the ResHF implementation. First, the $\mathcal{O}(N^5)$ computational scaling of the matrix adjugate formulation of ResHF needs to be reduced to make it affordable for NAMD simulations. We see several routes to reducing the scaling, including, as an example, a hybrid implementation that uses the conventional approach for determinant pairs with well-conditioned overlap matrices, and the adjugate approach only for pairs with ill-conditioned overlap matrices. On the other hand, a decomposition of ξ_{ijk} similar to the tensor train decomposition could also be used to reduce scaling. Finally, using restricted determinants instead of unrestricted determinants could also reduce the scaling of the ResHF implementation because an additional factor of σ_k could be factored out of the ξ_{ijk} term. A manuscript detailing the use of restricted determinants in ResHF is currently being prepared.

A more pressing concern is the difficulty of converging ResHF wavefunctions. Indeed, despite the $\mathcal{O}(N^5)$ scaling of the present implementation, we find that the convergence of ResHF is the limiting factor in our current implementation, not the cost. We see two important routes to improving the convergence of ResHF. First is to develop a more robust initial guess for the ResHF wavefunction, which we have observed plays an outsized role in the convergence of ResHF. Second is to apply second-order optimization techniques. All of the above-mentioned strategies are under investigation in our group.

There remain several open questions concerning the overall reliability of the ResHF method for excited states. The results presented here confirm that dynamical correlation will be essential to obtaining quantitatively accurate excitation energies with ResHF. That said, there may still be a role for ResHF in NAMD simulations even without dynamical correlation, just as CASSCF is still used in NAMD simulations despite having the same problem.

In closing, we note that the ResHF method shares many structural similarities with other nonorthogonal electronic structure methods, such as breathing orbital valence bond theory²⁰ and multistate density functional theory.²¹ Therefore, we hope the matrix adjugate approach to ResHF will help to push forward the practicality of these under-developed and newly-developed methods.

SUPPLEMENTAL MATERIAL

The Supplemental Material includes 4SA-ResHF(4sd) results for singlet-triplet gaps, a derivation of $\langle \hat{S}^2 \rangle$ for nonorthogonal Slater determinants, and plots of density differences.

ACKNOWLEDGMENTS

This work was supported by a startup fund from Case Western Reserve University and NSF CAREER award CHE-2236959. This work made use of the High Performance Computing Resource in the Core Facility for Advanced Research

Computing at Case Western Reserve University. E.R.M. was supported by the Molecular Sciences Software Institute under U.S. National Science Foundation Grant No. ACI-1547580.

DATA AVAILABILITY

The ResHF implementation used in this study is openly available at <https://gitlab.com/team-parker/yucca>. The code and data that support the findings of this study are openly available in “Numerically Stable Resonating Hartree-Fock with Matrix Adjugates” at <https://osf.io/ahnbp/>.

AUTHOR CONTRIBUTIONS

Ericka Roy Miller: conceptualization (supporting); data curation (lead); investigation (lead); formal analysis (lead); methodology (equal); software (lead); visualization (lead); writing - original draft (lead); writing - review and editing (equal). **Shane M. Parker:** conceptualization (lead); funding acquisition (lead); formal analysis (supporting); methodology (equal); resources (lead); software (supporting); supervision (lead); writing - review and editing (equal).

Appendix A: Applying Resolution-of-the-Identity to Resonating Fock Matrices

As detailed in Section II B, the bulk of the complexity in ResHF-adj is contained in the virtual, occupied block of the \mathbf{K}^{AB} matrix. Therefore, we will focus exclusively on Eq. (32) in the following analysis. In our implementation, we generally separate out \mathbf{K}^{AB} into four terms:

$$\mathbf{K}_{\text{uo}}^{AB} = \mathbf{A}_{\text{u}}^\dagger (\mathbf{K1} + \mathbf{K2} + \mathbf{K3} + \mathbf{K4}) \mathbf{A}_0 \quad (\text{A1a})$$

$$\mathbf{K1} = s_{AB} \mathbf{F}^{AB} \mathbf{Q}^{AB} \mathbf{S} \quad (\text{A1b})$$

$$\mathbf{K2} = -s_{AB} \mathbf{S} \mathbf{Q}^{AB} \mathbf{F}^{AB} \mathbf{Q}^{AB} \mathbf{S} \quad (\text{A1c})$$

$$\mathbf{K3} = H_{AB} \mathbf{S} \mathbf{Q}^{AB} \mathbf{S} \quad (\text{A1d})$$

$$\mathbf{K4} = -s_{AB} E_I \mathbf{S} \mathbf{Q}^{AB} \mathbf{S}. \quad (\text{A1e})$$

For the sake of organization, we will apply this same grouping throughout our discussion of the resolution-of-the-identity (RI) algorithms.

To streamline the equations in this section, we introduce Einstein notation and re-write Eq. (39) as

$$(pq|rs) \approx (pq|\tilde{P})(\tilde{P}|rs), \quad (\text{A2})$$

where

$$(pq|\tilde{P}) = (pq|Q)(L^{-1})_{QP} \quad (\text{A3})$$

and L_{PQ} comes from the Cholesky decomposition of the $(P|Q)$ matrix.

We collect here all the two electron components of Eq. (32) expressed using unrestricted spin MOs (see Appendix B) in

the biorthogonal SVD MO representation:

$$(K^{AB,\alpha})_{ai}^{2e-} = (K1^\alpha)_{ai}^{2e-} + (K2^\alpha)_{ai}^{2e-} + (K3^\alpha)_{ai}^{2e-} \quad (\text{A4a})$$

$$(K1^\alpha)_{ai}^{2e-} = \eta (a_A^\alpha i_B^\alpha | j_A^\beta j_B^\beta | \xi_i^\alpha \xi_j^\beta) + \eta \left| \Sigma^{AB,\beta} \right| (a_A^\alpha i_B^\alpha | j_A^\alpha j_B^\alpha | \xi_{ij}^\alpha) \quad (\text{A4b})$$

$$(K2^\alpha)_{ai}^{2e-} = -\eta \bar{S}_{aj}^{AB,\alpha} (j_A^\alpha i_B^\alpha | k_A^\beta k_B^\beta | \xi_{ij}^\alpha \xi_k^\beta) - \eta \left| \Sigma^{AB,\beta} \right| \bar{S}_{aj}^{AB,\alpha} (j_A^\alpha i_B^\alpha | k_A^\alpha k_B^\alpha | \xi_{ijk}^\alpha) \quad (\text{A4c})$$

$$(K3^\alpha)_{ai}^{2e-} = \eta \bar{S}_{ai}^{AB,\alpha} (j_A^\alpha j_B^\alpha | k_A^\beta k_B^\beta | \xi_{ij}^\alpha \xi_k^\beta) + \frac{1}{2} \eta \bar{S}_{ai}^{AB,\alpha} (j_A^\beta j_B^\beta | k_A^\alpha k_B^\alpha | \xi_i^\alpha \xi_j^\beta) + \frac{1}{2} \eta \left| \Sigma^{AB,\beta} \right| \bar{S}_{ai}^{AB,\alpha} (j_A^\alpha j_B^\alpha | k_A^\alpha k_B^\alpha | \xi_{ijk}^\alpha) \quad (\text{A4d})$$

We now present the RI algorithms used to compute each set of $(K^{AB,\alpha})_{ai}^{2e-}$ terms. For simplicity, we use T to denote a generic intermediate, and we do not highlight the use of common intermediates across different contributions. Furthermore, we show only the α component. The β component can be obtained by swapping α and β indices.

1. RI approximation of two-electron $\mathbf{K}_{\text{uo}}^{AB}$ Set 1 terms

Expressing the ERIs using auxiliary basis functions, we write Eq. (A4b) as

$$(K1^\alpha)_{ai}^{2e-} = \eta (a_A^\alpha i_B^\alpha | \tilde{P} | \tilde{P} | j_A^\beta j_B^\beta | \xi_i^\alpha \xi_j^\beta) + \eta \left| \Sigma^{AB,\beta} \right| (a_A^\alpha i_B^\alpha | \tilde{P} | \tilde{P} | j_A^\alpha j_B^\alpha | \xi_{ij}^\alpha) - \eta \left| \Sigma^{AB,\beta} \right| (a_A^\alpha j_B^\alpha | \tilde{P} | \tilde{P} | j_A^\alpha i_B^\alpha | \xi_{ij}^\alpha) \quad (\text{A5})$$

The first $(K1^\alpha)_{ai}^{2e-}$ term, the mixed-spin Coulomb contribution, is fully contracted over the spin MO indices prior to the final contraction step:

$$T_{aiP} \leftarrow \xi_i^\alpha (a_A^\alpha i_B^\alpha | \tilde{P}) \quad (\text{A6a})$$

$$T_P \leftarrow (\tilde{P} | j_A^\beta j_B^\beta | \xi_j^\beta) \quad (\text{A6b})$$

$$(K1^\alpha)_{ai}^{2e-} += \eta T_{aiP} T_P. \quad (\text{A6c})$$

For the second $(K1^\alpha)_{ai}^{2e-}$ term, the spin-pure Coulomb contribution, we are also able to fully contract over the spin MO indices in the intermediate step:

$$T_{Pi} \leftarrow (\tilde{P} | j_A^\alpha j_B^\alpha | \xi_{ij}^\alpha) \quad (\text{A7a})$$

$$(K1^\alpha)_{ai}^{2e-} += \eta (a_A^\alpha i_B^\alpha | \tilde{P}) T_{Pi}. \quad (\text{A7b})$$

$$(\text{A7c})$$

For the final $(K1^\alpha)_{ai}^{2e-}$ term, the exchange contribution, we are unable to fully contract over the spin MO indices in the intermediate step. Thus, the final contraction is between two Rank 3 tensors:

$$T_{Pji} \leftarrow (\tilde{P} | j_A^\alpha i_B^\alpha | \xi_{ij}^\alpha) \quad (\text{A8a})$$

$$(K1^\alpha)_{ai}^{2e-} -= \eta (a_A^\alpha j_B^\alpha | \tilde{P}) T_{Pji} \quad (\text{A8b})$$

2. RI approximation of two-electron $\mathbf{K}_{\text{uo}}^{AB}$ Set 2 terms

Expressing the ERIs using auxiliary basis functions, we write Eq. (A4c) as

$$(K2^\alpha)_{ai}^{2e-} = -\eta \bar{S}_{aj}^{AB,\alpha} (j_A^\alpha i_B^\alpha | \tilde{P} | \tilde{P} | k_A^\beta k_B^\beta | \xi_{ij}^\alpha \xi_k^\beta) - \eta \left| \Sigma^{AB,\beta} \right| \bar{S}_{aj}^{AB,\alpha} (j_A^\alpha i_B^\alpha | \tilde{P} | \tilde{P} | k_A^\alpha k_B^\alpha | \xi_{ijk}^\alpha) + \eta \left| \Sigma^{AB,\beta} \right| \bar{S}_{aj}^{AB,\alpha} (j_A^\alpha k_B^\alpha | \tilde{P} | \tilde{P} | k_A^\alpha i_B^\alpha | \xi_{ijk}^\alpha) \quad (\text{A9})$$

To compute the first $(K2^\alpha)_{ai}^{2e-}$ term, the mixed-spin Coulomb contribution, we first combine the overlap and ξ_{ij} terms, before proceeding with contractions involving the ERIs:

$$T_{aji} \leftarrow \bar{S}_{aj}^{AB,\alpha} \xi_{ij}^\alpha \quad (\text{A10a})$$

$$T_{aiP} \leftarrow T_{aji} (j_A^\alpha i_B^\alpha | \tilde{P}) \quad (\text{A10b})$$

$$T_P \leftarrow (\tilde{P} | k_A^\beta k_B^\beta | \xi_k^\beta) \quad (\text{A10c})$$

$$(K2^\alpha)_{ai}^{2e-} -= \eta T_{aiP} T_P. \quad (\text{A10d})$$

For the second $(K2^\alpha)_{ai}^{2e-}$ term, the spin-pure Coulomb contribution, we incorporate the overlap term via a Rank 4 tensor, before completing the tensor contraction with the other half ERI:

$$T_{ajjP} \leftarrow \bar{S}_{aj}^{AB,\alpha} (j_A^\alpha i_B^\alpha | \tilde{P}) \quad (\text{A11a})$$

$$T_{Pij} \leftarrow (\tilde{P} | k_A^\alpha k_B^\alpha | \xi_{ijk}^\alpha) \quad (\text{A11b})$$

$$(K2^\alpha)_{ai}^{2e-} -= \eta \left| \Sigma^{AB,\beta} \right| T_{ajjP} T_{Pij}. \quad (\text{A11c})$$

Finally, in the third $(K2^\alpha)_{ai}^{2e-}$ term, the exchange contribution is formed through the contraction of two Rank 4 tensors,

$$T_{ajkP} \leftarrow \bar{S}_{aj}^{AB,\alpha} (j_A^\alpha k_B^\alpha | \tilde{P}) \quad (\text{A12a})$$

$$T_{Pki} \leftarrow (\tilde{P} | k_A^\alpha i_B^\alpha | \xi_{ijk}^\alpha) \quad (\text{A12b})$$

$$(K2^\alpha)_{ai}^{2e-} += \eta \left| \Sigma^{AB,\beta} \right| T_{ajkP} T_{Pki}, \quad (\text{A12c})$$

making this the largest scaling step in Resonating Fock matrix builder routine at $O(N^5)$ with respect to the number of basis functions.

3. RI approximation of two-electron $\mathbf{K}_{\text{uo}}^{AB}$ Set 3 terms

Expressing the ERIs using auxiliary basis functions, we write Eq. (A4d) as

$$(K3^\alpha)_{ai}^{2e-} = \eta \bar{S}_{ai}^{AB,\alpha} (j_A^\alpha j_B^\alpha | \tilde{P} | \tilde{P} | k_A^\beta k_B^\beta | \xi_{ij}^\alpha \xi_k^\beta) + \frac{1}{2} \eta \bar{S}_{ai}^{AB,\alpha} \xi_i^\alpha (j_A^\beta j_B^\beta | \tilde{P} | \tilde{P} | k_A^\beta k_B^\beta | \xi_{jk}^\beta) - \frac{1}{2} \eta \bar{S}_{ai}^{AB,\alpha} \xi_i^\alpha (j_A^\beta k_B^\beta | \tilde{P} | \tilde{P} | k_A^\beta j_B^\beta | \xi_{jk}^\beta) + \frac{1}{2} \eta \left| \Sigma^{AB,\beta} \right| \bar{S}_{ai}^{AB,\alpha} (j_A^\alpha j_B^\alpha | \tilde{P} | \tilde{P} | k_A^\alpha k_B^\alpha | \xi_{ijk}^\alpha) - \frac{1}{2} \eta \left| \Sigma^{AB,\beta} \right| \bar{S}_{ai}^{AB,\alpha} (j_A^\alpha k_B^\alpha | \tilde{P} | \tilde{P} | k_A^\alpha j_B^\alpha | \xi_{ijk}^\alpha) \quad (\text{A13})$$

For the first term in $(K3^\alpha)^{2e-}$, the mixed-spin Coulomb contribution, we are able to fully contract over the spin MO indices before the final contraction step:

$$T_{iP} \leftarrow \xi_{ij}^\alpha (j_A^\alpha j_B^\alpha | \tilde{P}) \quad (\text{A14a})$$

$$T_P \leftarrow (\tilde{P} | k_A^\beta k_B^\beta) \xi_k^\beta \quad (\text{A14b})$$

$$(K3^\alpha)^{2e-} += \eta \bar{S}_{ai}^{AB,\alpha} T_{iP} T_P. \quad (\text{A14c})$$

For the second term in $(K3^\alpha)^{2e-}$, the β spin Coulomb contribution, we contract the half ERIs into Rank 2 tensors before fully contracting with the ξ_{jk} term to produce a scalar, which is then used to scale the final operation:

$$T_{jP} \leftarrow (j_A^\alpha j_B^\alpha | \tilde{P}) \quad (\text{A15a})$$

$$T_{Pk} \leftarrow (\tilde{P} | k_A^\alpha k_B^\alpha) \quad (\text{A15b})$$

$$T_{jk} \leftarrow T_{jP} T_{Pk} \quad (\text{A15c})$$

$$T \leftarrow T_{jk} \xi_{jk}^\beta \quad (\text{A15d})$$

$$(K3^\alpha)^{2e-} += \frac{1}{2} \eta \bar{S}_{ai}^{AB,\alpha} \xi_i^\alpha T. \quad (\text{A15e})$$

We apply a similar strategy for the third term in $(K3^\alpha)^{2e-}$, the β spin exchange contribution, albeit contracting Rank 3 tensors to produce the scalar, which is then used in the final operation:

$$T_{Pkj} \leftarrow (\tilde{P} | k_A^\beta j_B^\beta) \xi_{jk}^\beta \quad (\text{A16a})$$

$$T \leftarrow (j_A^\beta k_B^\beta | \tilde{P}) T_{Pkj} \quad (\text{A16b})$$

$$(K3^\alpha)^{2e-} -= \frac{1}{2} \eta \bar{S}_{ai}^{AB,\alpha} \xi_i^\alpha T. \quad (\text{A16c})$$

For the fourth term in $(K3^\alpha)^{2e-}$, the α spin Coulomb contribution, we again contract the half ERIs into Rank 2 tensors before contracting with the ξ_{ijk} and overlap terms sequentially:

$$T_{jP} \leftarrow (j_A^\alpha j_B^\alpha | \tilde{P}) \quad (\text{A17a})$$

$$T_{Pk} \leftarrow (\tilde{P} | k_A^\alpha k_B^\alpha) \quad (\text{A17b})$$

$$T_{jk} \leftarrow T_{jP} T_{Pk} \quad (\text{A17c})$$

$$T_i \leftarrow \xi_{ijk}^\alpha T_{jk} \quad (\text{A17d})$$

$$(K3^\alpha)^{2e-} += \frac{1}{2} \eta \left| \Sigma^{AB,\beta} \right| \bar{S}_{ai}^{AB,\alpha} T_i. \quad (\text{A17e})$$

Finally, to resolve the fifth term in $(K3^\alpha)^{2e-}$, the α spin exchange contribution, we contract the ERIs via a Rank 4 tensor and a Rank 3 tensor before the final contraction with the overlap term:

$$T_{Pijk} \leftarrow (\tilde{P} | k_A^\alpha j_B^\alpha) \xi_{ijk}^\alpha \quad (\text{A18a})$$

$$T_i \leftarrow (j_A^\alpha k_B^\alpha | \tilde{P}) T_{Pijk} \quad (\text{A18b})$$

$$(K3^\alpha)^{2e-} -= \frac{1}{2} \eta \left| \Sigma^{AB,\beta} \right| \bar{S}_{ai}^{AB,\alpha} T_i. \quad (\text{A18c})$$

Appendix B: ResHF intermediates with unrestricted orbitals

In the following treatment, we will express equations using unrestricted molecular orbitals,

$$\phi_p^{A,\omega}(\mathbf{x}_1) = s(\omega) \psi_p^{A,\omega}(\mathbf{r}_1) \quad (\text{B1})$$

where we have defined a generic spin index, $\omega = \alpha, \beta$, and $\psi_p^{A,\omega}$ is a spatial MOs corresponding to ω spin electrons. The MO overlap matrix of Eq. (8) becomes a diagonal block matrix with elements

$$\mathbf{S}^{AB,\omega} = \mathbf{C}^{A,\omega,\dagger} \mathbf{S} \mathbf{C}^{B,\omega}, \quad (\text{B2})$$

and the interdeterminant overlap can be separated into α and β components as

$$s_{AB} = |\mathbf{S}_{oo}^{AB,\alpha}| |\mathbf{S}_{oo}^{AB,\beta}| = \eta \left[\prod_i^{N_\alpha} \sigma_i^\alpha \right] \left[\prod_j^{N_\beta} \sigma_j^\beta \right], \quad (\text{B3})$$

where two sets of singular values, σ_i^ω , are distinguished based on spin and $\eta = |\mathbf{U}^{AB,\alpha}(\mathbf{V}^{AB,\alpha})^\dagger| |\mathbf{U}^{AB,\beta}(\mathbf{V}^{AB,\beta})^\dagger| = \pm 1$.

The interdeterminant density matrix of Eq. (9) also becomes block diagonal with respect to spin, with elements

$$\gamma^{AB,\omega} = s_{AB} \mathbf{Q}^{AB,\omega}. \quad (\text{B4})$$

Using this, we can write the coupling matrix element from Eq. (11) as

$$H_{AB} = s_{AB} \sum_\omega \left[\langle \mathbf{h} \mathbf{Q}^{AB,\omega} \rangle + \frac{1}{2} \langle \mathbf{G}^{AB,\omega} \mathbf{Q}^{AB,\omega} \rangle \right], \quad (\text{B5})$$

where

$$\mathbf{G}_{\mu\nu}^{AB,\omega} = \sum_{\lambda\sigma} (\mu\nu | \lambda\sigma) \mathcal{Q}_{\sigma\lambda}^{AB,\omega} + \sum_{\lambda\sigma} (\mu\nu | \lambda\sigma) \mathcal{Q}_{\sigma\lambda}^{AB,\omega'}, \quad (\text{B6})$$

where $\omega \neq \omega'$ and the electron repulsion integrals (ERIs) are now spatial integrals, defined as

$$(\mu\nu | \lambda\sigma) = \iint d\mathbf{r}_1 d\mathbf{r}_2 \chi_\mu^*(\mathbf{r}_1) \chi_\nu(\mathbf{r}_1) r_{12}^{-1} \chi_\lambda^*(\mathbf{r}_2) \chi_\sigma(\mathbf{r}_2). \quad (\text{B7})$$

We can also render the AO basis \mathbf{K}^{AB} matrix from Eq. (16) into a block diagonal matrix with elements

$$\mathbf{K}^{AB,\omega} = s_{AB} (\mathbf{1} - \mathbf{S} \mathbf{Q}^{AB,\omega}) \mathbf{F}^{AB,\omega} \mathbf{Q}^{AB,\omega} \mathbf{S} + (H_{AB} - s_{AB} E_I) \mathbf{S} \mathbf{Q}^{AB,\omega} \mathbf{S}, \quad (\text{B8})$$

where $\mathbf{F}^{AB,\omega} = \mathbf{h} + \mathbf{G}^{AB,\omega}$.

¹M. Richter, P. Marquetand, J. González-Vázquez, I. Sola, and L. González, J. Phys. Chem. Lett. **3**, 3090 (2012).

²T. Penfold, R. Spesyvtsev, O. M. Kirkby, R. S. Minns, D. S. N. Parker, H. H. Fielding, and G. A. Worth, J. Chem. Phys. **137**, 204310 (2012).

³B. F. E. Curchod, A. Sisto, and T. J. Martínez, J. Phys. Chem. A **121**, 265 (2017).

⁴T. Nelson, S. Fernandez-Alberti, A. E. Roitberg, and S. Tretiak, Acc. Chem. Res. **47**, 1155 (2014).

- ⁵K. D. Borne, J. C. Cooper, M. N. R. Ashfold, J. Bachmann, S. Bhat-tacharyya, R. Boll, M. Bonanomi, M. Bosch, C. Callegari, M. Centurion, M. Coreno, B. F. E. Curchod, M. B. Danailov, A. Demidovich, M. Di Fraia, B. Erk, D. Faccialà, R. Feifel, R. J. G. Forbes, C. S. Hansen, D. M. P. Holland, R. A. Ingle, R. Lindh, L. Ma, H. G. McGhee, S. B. Muvva, J. P. F. Nunes, A. Odate, S. Pathak, O. Plekan, K. C. Prince, P. Rebernik, A. Rouzée, A. Rudenko, A. Simoncig, R. J. Squibb, A. S. Venkatachalam, C. Vozzi, P. M. Weber, A. Kirrander, and D. Rolles, *Nat. Chem.* **16**, 499 (2024).
- ⁶M. S. Schuurman and A. Stolow, *Annu. Rev. Phys. Chem.* **69**, 427 (2018).
- ⁷J. Janoš and P. Slavíček, *J. Chem. Theory Comput.* **19**, 8273 (2023).
- ⁸T. V. Papineau, D. Jacquemin, and M. Vacher, *J. Phys. Chem. Lett.* **15**, 636 (2024).
- ⁹S. Mukherjee, R. S. Mattos, J. M. Toldo, H. Lischka, and M. Barbatti, *J. Chem. Phys.* **160**, 154306 (2024).
- ¹⁰B. G. Levine, C. Ko, J. Quenneville, and T. J. Martínez, *Mol. Phys.* **104**, 1039 (2006).
- ¹¹J. T. Taylor, D. J. Tozer, and B. F. E. Curchod, *J. Chem. Phys.* **159**, 214115 (2023).
- ¹²J. T. Taylor, D. J. Tozer, and B. F. E. Curchod, *J. Phys. Chem. A* **128**, 5314 (2024).
- ¹³M. Segado, I. Gómez, and M. Reguero, *Phys. Chem. Chem. Phys.* **18**, 6861 (2016).
- ¹⁴L. N. Tran and E. Neuscammann, *J. Phys. Chem. A* **124**, 8273 (2020).
- ¹⁵A. Marie and H. G. A. Burton, *J. Phys. Chem. A* **127**, 4538 (2023).
- ¹⁶S. Saade and H. G. A. Burton, *J. Chem. Theory Comput.* **20**, 5105 (2024).
- ¹⁷B. Bremond, *Nuc. Phys.* **58**, 687 (1964).
- ¹⁸H. Fukutome, *Prog. Theor. Phys.* **80**, 417 (1988).
- ¹⁹H. G. A. Burton and A. J. W. Thom, *J. Chem. Theory Comput.* **15**, 4851 (2019).
- ²⁰P. C. Hiberty and S. Shaik, *Theor. Chem. Acc.* **108**, 255 (2002).
- ²¹Y. Lu and J. Gao, *J. Phys. Chem. Lett.* **13**, 7762 (2022).
- ²²J. Olsen, *J. Chem. Phys.* **143**, 114102 (2015).
- ²³C. Sun, F. Gao, and G. E. Scuseria, *J. Chem. Theory Comput.* **20**, 3741 (2024).
- ²⁴C. A. Jiménez-Hoyos, R. Rodríguez-Guzmán, and G. E. Scuseria, *J. Chem. Phys.* **139**, 224110 (2013).
- ²⁵J. Nite and C. A. Jiménez-Hoyos, *J. Chem. Theory Comput.* **15**, 5343 (2019).
- ²⁶A. D. Mahler and L. M. Thompson, *J. Chem. Phys.* **154**, 244101 (2021).
- ²⁷R. D. Hill and E. E. Underwood, *SIAM. J. on Algebraic and Discrete Meth-ods* **6**, 731 (1985).
- ²⁸G. W. Stewart, *Linear Algebra and its Applications* **283**, 151 (1998).
- ²⁹H. Koch and E. Dalgaard, *Chem. Phys. Lett.* **212**, 193 (1993).
- ³⁰G. P. Chen and G. E. Scuseria, *J. Chem. Phys.* **158**, 231102 (2023).
- ³¹S. M. Parker, “Yucca,” <https://gitlab.com/team-parker/yucca> (2024).
- ³²H. G. A. Burton, *J. Chem. Phys.* **154**, 144109 (2021).
- ³³R. Broer and W. C. Nieuwpoort, *Theoret. Chim. Acta* **73**, 405 (1988).
- ³⁴E. J. Baerends, D. E. Ellis, and P. Ros, *Chem. Phys.* **2**, 41 (1973).
- ³⁵B. I. Dunlap, J. W. D. Connolly, and J. R. Sabin, *J. Chem. Phys.* **71**, 3396 (1979).
- ³⁶F. Weigend, *Phys. Chem. Chem. Phys.* **4**, 4285 (2002).
- ³⁷F. Neese, *WIREs Comput. Mol. Sci.* **12**, e1606 (2022).
- ³⁸E. R. Miller and S. M. Parker, “Numerically stable resonating hartree-fock with matrix adjugates,” <https://osf.io/ahnbp/> (2024).
- ³⁹C. Kollmar, K. Sivalingam, B. Helmich-Paris, C. Angeli, and F. Neese, *J. Comp. Chem.* **40**, 1463 (2019).
- ⁴⁰P. Pulay, *J. Comp. Chem.* **3**, 556 (1982).
- ⁴¹F. Weigend and R. Ahlrichs, *Phys. Chem. Chem. Phys.* **7**, 3297 (2005).
- ⁴²T. H. Dunning, *J. Chem. Phys.* **90**, 1007 (1989).
- ⁴³R. A. Kendall, T. H. Dunning, and R. J. Harrison, *J. Chem. Phys.* **96**, 6796 (1992).
- ⁴⁴F. Weigend, F. Furche, and R. Ahlrichs, *J. Chem. Phys.* **119**, 12753 (2003).
- ⁴⁵P.-A. Malmqvist and B. O. Roos, *Chem. Phys. Lett.* **155**, 189 (1989).
- ⁴⁶L. R. Kahn, P. J. Hay, and I. Shavitt, *J. Chem. Phys.* **61**, 3530 (1974).
- ⁴⁷J. Bauschlicher, Charles W. and S. R. Langhoff, *J. Chem. Phys.* **89**, 4246 (1988).
- ⁴⁸M. Ben-Nun and T. J. Martínez, *Chem. Phys.* **259**, 237 (2000).
- ⁴⁹D. Feller, K. A. Peterson, and E. R. Davidson, *J. Chem. Phys.* **141**, 104302 (2014).
- ⁵⁰M. Ben-Nun and T. J. Martínez, *Chem. Phys. Lett.* **298**, 57 (1998).
- ⁵¹P.-F. Loos, A. Scemama, A. Blondel, Y. Garniron, M. Caffarel, and D. Jacquemin, *J. Chem. Theory Comput.* **14**, 4360 (2018).
- ⁵²P.-F. Loos, F. Lipparini, M. Boggio-Pasqua, A. Scemama, and D. Jacquemin, *J. Chem. Theory Comput.* **16**, 1711 (2020).
- ⁵³P.-F. Loos and D. Jacquemin, *J. Phys. Chem. A* **125**, 10174 (2021).
- ⁵⁴S. J. Stoneburner, D. G. Truhlar, and L. Gagliardi, *J. Chem. Phys.* **148**, 064108 (2018).
- ⁵⁵F. Bettanin, L. F. A. Ferrão, M. J. Pinheiro, A. J. A. Aquino, H. Lischka, F. Machado, and D. Nachtigallova, *J. Chem. Theory Comput.* **13**, 4297 (2017).
- ⁵⁶D. Khokhlov and A. Belov, *J. Phys. Chem. A* **124**, 5790 (2020).